

Optical Charge Injection and Full Coherent Control of Spin-Qubit in the Telecom C-band Emitting Quantum Dot

Lukasz Dusanowski,^{1,2,*} Cornelius Nawrath,³ Simone L. Portalupi,³ Michael Jetter,³ Tobias Huber,¹ Sebastian Klemmt,¹ Peter Michler,³ and Sven Höfling^{1,4}

¹*Technische Physik and Würzburg-Dresden Cluster of Excellence ct.qmat, University of Würzburg, Physikalisches Institut and Wilhelm-Conrad-Röntgen-Research Center for Complex Material Systems, Am Hubland, D-97074 Würzburg, Germany*

²*currently at: Department of Electrical Engineering, Princeton University, Princeton, NJ 08544, USA*

³*Institut für Halbleiteroptik und Funktionelle Grenzflächen (IHFG), Center for Integrated Quantum Science and Technology (IQST) and SCoPE, University of Stuttgart, D-70569 Stuttgart, Germany*

⁴*SUPA, School of Physics and Astronomy, University of St Andrews, KY16 9SS St Andrews, UK*

Solid-state quantum emitters with manipulable spin-qubits are promising platforms for quantum communication applications. Although such light-matter interfaces could be realized in many systems only a few allow for light emission in the telecom bands necessary for long-distance quantum networks. Here, we propose and implement a new optically active solid-state spin-qubit based on a hole confined in a single InAs/GaAs quantum dot grown on an InGaAs metamorphic buffer layer emitting photons in the C-band. We lift the hole spin-degeneracy using an external magnetic field and demonstrate hole injection, initialization, read-out and complete coherent control using picosecond optical pulses. These results showcase a new solid-state spin-qubit platform compatible with preexisting optical fibre networks.

Keywords: spin control, hole qubit, quantum dot, telecom C-band

Long-distance quantum network technologies require reliable interfaces between stationary qubits and photons with frequencies in the telecom bands [1, 2]. In this regard, spin degrees of freedom in solid-state quantum emitters are of particular interest due to the potential of realizing quantum entanglement between a confined spin and a propagating photon [3–6]. Spin-based photonics have been to date realized using a wide range of material systems. Each platform varies in the terms of electronic structure, emission wavelength, optical performance, spin-coherence and integration capabilities with photonic devices [7, 8]. Semiconductor quantum dots (QDs) for instance, show excellent optical properties [9, 10], achieve spin coherence times on the level of tens of microseconds [11, 12], and allow for efficient generation of spin-photon [4–6, 13] and spin-spin [14, 15] entanglement. Another well-established spin-system, vacancy centres in diamond, while suffering intrinsically low emission efficiency into the zero-phonon-line, show very long coherence times on the level of single seconds [16], and allowed for demonstration of spin-spin entanglement on the record distance of 1.3 km [17]. While diamond is still a rather challenging material for micro-processing, platforms based on defects in SiC show similar optical-performance with milliseconds spin coherence times [18, 19], and stand out by maturity of SiC growth and processing methods. Another promising class of spin-active emitters are rare-earth-ion doped crystals embedded in cavities [20–22]. Such systems might in principle achieve over seconds spin coherence times [23], but require the usage of high-finesse cavities to enhance the

intrinsically slow emission rates.

Among those many types of solid-state platforms, only a few systems demonstrated capability of directly interfacing spins with telecom-wavelength photons. Recently, spin-control has been demonstrated at 1220 nm wavelength in nitrogen-vacancy centers in SiC [24], at 1330 nm using ensemble of radiation T damage centers in ²⁸Si [25], and at 1550 nm in *Er*³⁺ in Y₂SiO₅ [21, 22]. In particular, the latter system operates in the lowest-loss telecom C-band centered at 1550 nm, promising a clear advantage for long-distance quantum communication applications [2]. Emitters with transitions incompatible with fibre networks, such as defects in diamond, could potentially take advantage of quantum frequency conversion into telecom wavelengths [4, 26]. While such an approach offers flexibility in terms of frequency matching of multiple emitters [27], it is intrinsically limited by the efficiency of the frequency conversion process and requires a considerable technological overhead.

In this work, we introduce a new spin-qubit system based on a single hole confined in a semiconductor self-assembled QD emitting radiation directly in the telecom C-band. We demonstrate the full set of spin-control operations consisting of spin injection, initialization, read-out and coherent rotation. We perform all protocols at 76 MHz repetition rate, where the spin-rotation is achieved on the picosecond time-scale using detuned optical pulses. This demonstration provides a clear pathway towards direct spin-photon entanglement in the telecom C-band for applications in long-distance quantum communication. Thanks to the QDs' intrinsically short ra-

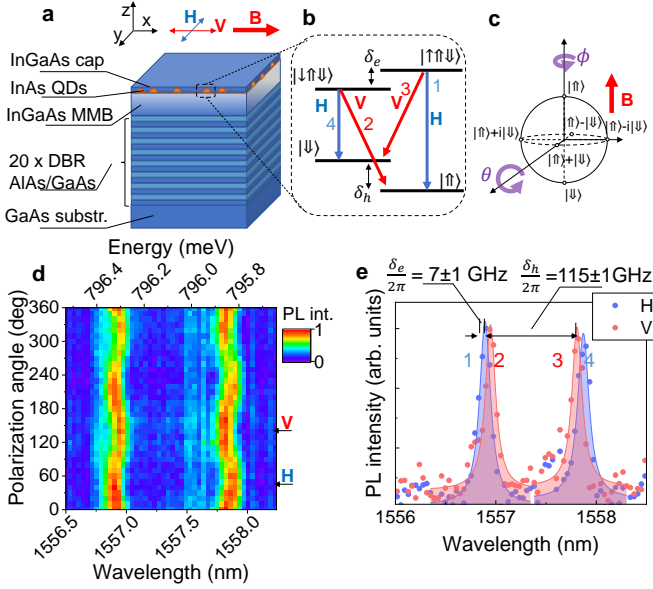


FIG. 1. **Quantum dot spin platform.** **a**, Sample layer structure and geometry used (not to scale). A single layer of InAs quantum dots is grown on an InGaAs metamorphic buffer (MMB) layer allowing for emission in the C-band telecom window. Bottom distributed Bragg reflectors (DBR, 20 pairs) and air top interface nominally form a $3\text{-}\lambda$ cavity for increased photon collection efficiency. An external magnetic field (B) is applied along the x -axis (Voigt geometry). Emission collection and excitation is performed along the z -axis. Insets: orientation (x, y, z) and polarization convention (H, V) used. **b**, Trion level structure in Voigt magnetic field with radiative transitions selection rules, as used in the experiment. **c**, Bloch sphere representing the spin-qubit. **d**, Colour-coded map of the trion photoluminescence spectra as a function of detected polarization angle at 3 T magnetic field in Voigt configuration. **e**, Trion photoluminescence spectra at $B = 3$ T at horizontal (H) and vertical (V) linear polarization.

diative lifetimes of around 1 ns, our system provides a direct alternative to $E\text{r}^{3+}$ ions or platforms relying on frequency conversion.

Spin system under investigation. The physical system used in our experiment is presented in Fig. 1a. It consists of InAs quantum dots grown on an InGaAs metamorphic buffer (MMB) layer, reducing the lattice mismatch between the QDs and the underneath material [28]. This results in an emission wavelength in the telecom C-band. In addition, the QDs and the MMB are placed on a near lattice-matched AlAs/GaAs distributed Bragg reflector (DBR) that significantly enhances the photon extraction efficiency (see Methods). For optical experiments, we cool-down the sample to 1.6 K temperature and focus on a single QD by using a confocal microscope. Under non-resonant optical excitation, sharp emission lines are identified in photoluminescence spectra stemming from radiative recombination of various excitonic complexes. For this study, we preselect an isolated emitter with a single transition originating from

a charged exciton (see Supplementary Information S2). We attribute the investigated complex to a positive trion formed by a single electron and two holes [29].

Under a magnetic field oriented in Voigt geometry (perpendicular to the growth direction/optical axis), two Λ -systems are formed from an initial two-level system, where each optically active trion state $|\downarrow\uparrow\downarrow\rangle/|\uparrow\uparrow\downarrow\rangle$ is coupled to each of two ground hole spin states $|\downarrow\rangle$ and $|\uparrow\rangle$. The optical selection rules are indicated in Fig. 1b. In this work, we define a qubit as a quantum dot hole spin state $\cos(\theta/2)|\downarrow\rangle + e^{i\phi}\sin(\theta/2)|\uparrow\rangle$, which can be schematically represented on the Bloch sphere, where θ and ϕ are spherical co-ordinates as shown in Fig. 1c. The north and south pole represent the pure $|\downarrow\rangle$ and $|\uparrow\rangle$ states. Access to any arbitrary Bloch vector on the sphere requires the ability of spin rotation along two perpendicular axes to control both θ and ϕ angle.

In Fig. 1d polarization dependence of the preselected trion photoluminescence at 3 T magnetic field in Voigt configuration is shown. The emission spectrum shows a four-fold splitting, with polarized transitions consistent with selection rules shown in Fig. 1b. By fitting the emission peaks at vertical (V) and horizontal (H) polarization (as defined in Fig. 1) we recover the trion and hole splitting of 7 ± 1 GHz and 115 ± 1 GHz, respectively. Systematic investigation of the peaks in the function of the magnetic field reveal the ground spin-state and trion spin-state g -factors of 2.7 and 0.16, respectively (see Supplementary Information S3).

Optical charge injection. Within the current study, we utilize a nominally undoped QD sample, thus most of the QDs are uncharged. Interestingly, trion transitions are visible under non-resonant pumping, suggesting that photo-excited electrons and holes relax with different rates predominantly forming positive trion states. This, in turn, could be utilized to load the QD with a single charge, since directly after trion recombination the QD is left in the ground hole state. Moreover, since trions can recombine with equal probability into both spin states, such a charge injection scheme randomizes the initial spin-configuration serving additionally as an active-spin-reset.

To experimentally demonstrate the optical charge injection, we perform a two-colour pulse experiment as schematically described in Fig. 2a. First, we excite a QD with a 2 ps width non-resonant pulse at 850 nm to form a trion (1-2). Upon radiative recombination (3), the QD is left with single hole in random $|\downarrow\rangle$ or $|\uparrow\rangle$ spin configuration (4). After 4.5 ns we send another H-polarized pulse with 100 ps width and central wavelength of 1558nm, which is resonant with the $|\downarrow\rangle\text{-}|\downarrow\uparrow\downarrow\rangle$ transition (5). Taken, that a charge was indeed loaded into the QD, the second pulse should excite the system into the $|\downarrow\uparrow\downarrow\rangle$ trion state (6), which will then recombine radiatively (7). By spectrally filtering the diagonal V-polarized transition $|\downarrow\uparrow\downarrow\rangle\text{-}|\uparrow\rangle$ and performing a

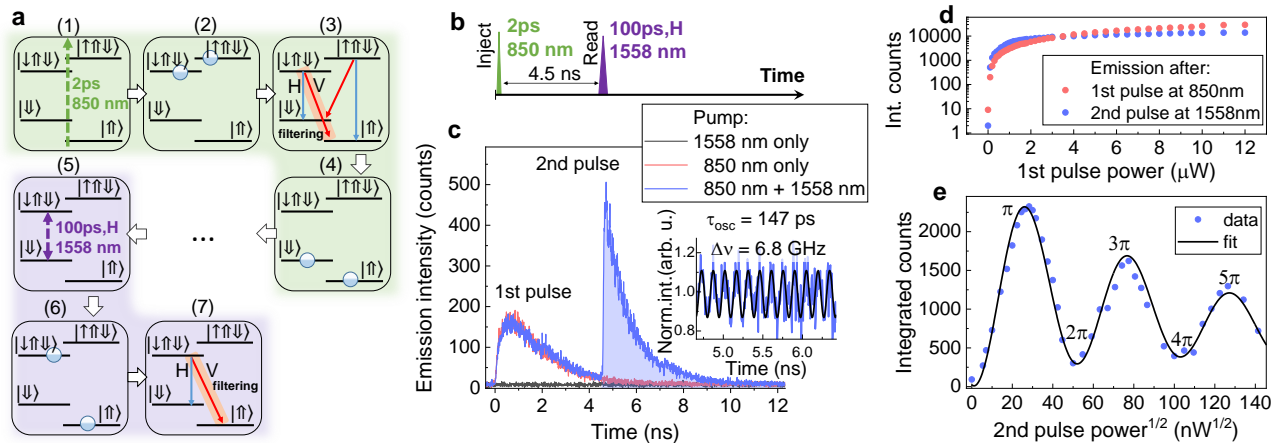


FIG. 2. **Charge injection and coherent control of trion state.** **a**, Schematic description of optical charge injection (1-4) and coherent control of trion state (5-7) used in the experiment. First, (1) a non-resonant pulse excites carriers in the semiconductor which then relax (2) forming a trion state with random spin configuration. Next, (3) the trion recombines radiatively (4) leaving the QD with a charge in a random spin configuration $|\downarrow\rangle$ or $|\uparrow\rangle$ state. (5) The second pulse at H polarization resonant with $|\downarrow\rangle-|\downarrow\uparrow\downarrow\rangle$ transition excites the system into (6) $|\downarrow\uparrow\downarrow\rangle$ trion state which can then recombine radiatively emitting an H or V-polarized photon. In the experiment the V-polarized $|\downarrow\uparrow\downarrow\rangle-|\uparrow\rangle$ transition is filtered spectrally and detected. **b**, The excitation pulse sequence used in the experiment. The first pulse at 850 nm injects the carrier into the QD and a second pulse at 1558 nm resonantly excites the system into the $|\downarrow\uparrow\downarrow\rangle$ state. **c**, Time-trace of $|\downarrow\uparrow\downarrow\rangle-|\uparrow\rangle$ emission after non-resonant pulse only (red curve), resonant pulse only (black curve) and both pulses (blue curve). Emission after resonant pulse exhibits slight amplitude oscillations with a period of 147 ± 1 ps corresponding to the $|\downarrow\uparrow\downarrow\rangle-|\uparrow\rangle$ states splitting. Inset: Intensity oscillations recovered from the time-trace. **d**, Integrated emission counts after 1st (non-resonant) and 2nd (resonant) excitation pulse in the function of 1st (non-resonant) pulse power. **e**, Integrated emission counts after 2nd (resonant) pulse in the function of the square root of the 2nd (resonant) pulse power. The emission exhibits clear Rabi oscillations up to 5π pulse area.

time-resolved measurement, we can trace the QD emission dynamics following both pulses, as shown in Fig. 2c. Emission decay after the first pulse exhibits a mono-exponential decay with a time constant of 1.4 ns, as typically observed for such type of QDs [28]. Emission after the second pulse exhibits a similar mono-exponential decay, however, with a slight amplitude oscillation with a period of 147 ± 1 ps as indicated in the Fig. 2c inset. This oscillations period corresponds to a 6.80 ± 0.05 GHz frequency which is in good agreement with trion state splitting of 7 ± 1 GHz and is a fingerprint of coherent excitation. Interestingly, when the sample is excited with the resonant pulse only, emission from the QD is not observed (black curve). This allows recording the reference background time-trace related to the scattered laser. By integration of the counts corresponding to the first or second decay on the graph (blue area), we can plot the time-integrated intensity of the QD emission after each pulse. In Fig. 2d the emission intensity after each excitation pulse is plotted as a function of the first (charge injection) pulse power. Clear intensity increase and saturation at around $1 \mu\text{W}$ are observed for both decays. In Fig. 2e we plot the emission after the second (resonant) pulse as a function of the square root of the second pulse power. In this case, clear oscillatory behavior is observed related to coherent Rabi rotation of trion state population. We can observe rotation up to 5π -pulse area, which

is clear evidence of coherent trion control.

Spin initialization. To initialize the spin into the desired $|\downarrow\rangle/|\uparrow\rangle$ state we use optical pumping [30, 31]. For that a continuous wave (cw) laser at H polarization is tuned into resonance with the transition $|\uparrow\rangle-|\uparrow\uparrow\downarrow\rangle/|\downarrow\rangle-|\downarrow\uparrow\downarrow\rangle$ (brown arrows in Fig. 3a and b inset). The fluorescence is monitored at the corresponding V-polarized transitions $|\uparrow\uparrow\downarrow\rangle-|\downarrow\rangle/|\downarrow\uparrow\downarrow\rangle-|\uparrow\rangle$. A significant increase of the emission intensity is observed when the resonance with the given transition is established as shown in Fig. 3a and b. After a charge is injected into the QD by the non-resonant pulse, the cw pumping laser re-excites the $|\uparrow\rangle$ state into $|\uparrow\uparrow\downarrow\rangle$, until the event of V-polarized emission, which will initialize the system into $|\downarrow\rangle$. Analogously, by optical pumping of the transition $|\downarrow\rangle-|\downarrow\uparrow\downarrow\rangle$, the system can be initialized in the $|\uparrow\rangle$ state. Since the probability of V and H-polarized fluorescence is equal, the initialization process will require few emission cycles to reach high fidelity. Based on our simulations, we expect that within 4.5 ns (6 ns) initialization time we can reach 96% (99%) spin preparation fidelity (see Supplementary Information S4).

To read the spin state in the QD we send a subsequent H-polarized pulse resonant with $|\downarrow\rangle-|\downarrow\uparrow\downarrow\rangle$, which probes the $|\downarrow\rangle$ state population (pulse sequence shown in Fig. 3c). In the case of the $|\downarrow\rangle$ initialization, around two-fold enhancement of the emission intensity can be

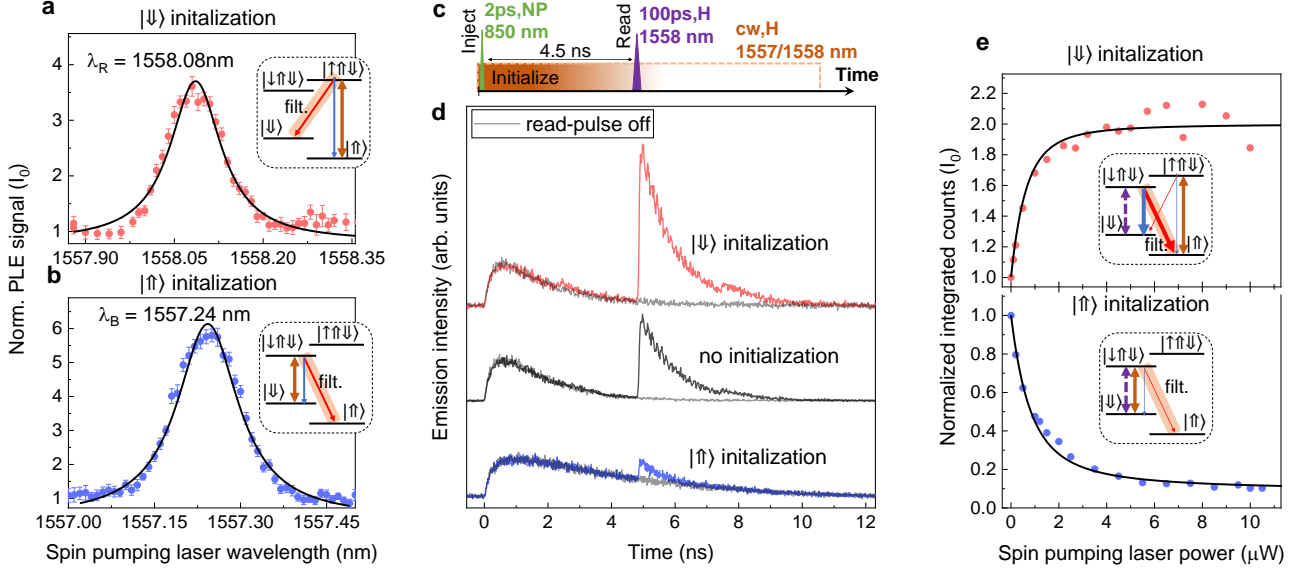


FIG. 3. **Spin initialization by optical pumping.** **a,b**, The emission intensity of $|\uparrow\uparrow\downarrow\rangle-|\downarrow\rangle$ and $|\downarrow\uparrow\downarrow\rangle-|\uparrow\rangle$ transition as a function of spin pumping laser wavelength scanned along the $|\uparrow\uparrow\downarrow\rangle-|\uparrow\rangle$ and $|\downarrow\uparrow\downarrow\rangle-|\downarrow\rangle$ transition, respectively. The signal is normalized to intensity in the absence of spin-pumping laser. Insets: Trion level schemes with relevant transitions. **c**, Pulse sequence used for demonstration of $|\uparrow\rangle$ and $|\downarrow\rangle$ spin initialization and subsequent spin read-out. First (non-resonant) pulse injects the carriers into the QD with random spin configuration. Then the cw spin pumping laser initializes the system into $|\uparrow\rangle$ and $|\downarrow\rangle$. After 4.5 ns an H-polarized pulse resonant with $|\downarrow\rangle-|\downarrow\uparrow\downarrow\rangle$ probes the $|\downarrow\rangle$ state by exciting it into $|\downarrow\uparrow\downarrow\rangle$. **d**, Time-trace of $|\downarrow\uparrow\downarrow\rangle-|\uparrow\rangle$ emission demonstrating successful $|\downarrow\rangle$ and $|\uparrow\rangle$ initialization visible by increased and decreased emission intensity after a second (probe) pulse. **e**, The emission intensity of $|\downarrow\uparrow\downarrow\rangle-|\uparrow\rangle$ transition as a function of spin-pumping laser power normalized to the intensity observed in the absence of spin pumping. The data are fitted with a 4-level rate equation model. Insets: Trion level schemes with relevant transitions.

observed, while in the case of $|\uparrow\rangle$ initialization clear suppression is visible as shown in Fig. 3d. In the case of $|\uparrow\rangle$ pumping a re-excitation process is visible directly in the time-trace as a prolongation of the emission decay after the non-resonant pulse. In Fig. 3e integrated counts corresponding to the read-out pulse are plotted as a function of the spin pumping laser power in case of the $|\downarrow\rangle$ and $|\uparrow\rangle$ initialization, respectively. For the $|\downarrow\rangle$ pumping, the emission intensity reaches double the counts observable in case of no initialization, which is related to the increase of the $|\downarrow\rangle$ state preparation probability from 50% to almost 100%. In analogy, in the case of $|\uparrow\rangle$ pumping, significant suppression of the signal is observed. For spin pumping powers above $10 \mu\text{W}$, a spin-preparation fidelity of $94.5 \pm 0.5\%$ is achieved for 4.5 ns optical pumping time. This could be further improved by increasing the delay between charge injection and spin-read-out pulses.

Coherent control of the hole spin. For coherent rotation of the hole spin-state to any desired point on the Bloch sphere we employ detuned circularly polarized laser pulses [32]. If the laser detuning Δ is much larger than the splitting between the hole ground states δ_h , the net effect on the double Λ system is such that the population of the spin state should oscillate with an effective Rabi frequency Ω_{eff} , without physically exciting the system into the trion state. By keeping the pulse

length constant and by controlling its power, it is possible to coherently rotate the spin state between $|\downarrow\rangle$ and $|\uparrow\rangle$. The rotation angle θ will be in such case proportional to the square root of the detuned laser power and inversely proportional to the detuning [32].

For spin control experiments we apply a magnetic field of 1.5 T, decreasing the hole spin splitting to 57 GHz and increasing the Larmor precession period to around 17.5 ps. First, we send a non-resonant 850 nm charge injection pulse and initialize the system into the $|\uparrow\rangle$ state by optical pumping. Then, after around 6 ns we send a circularly polarized ~ 400 GHz red detuned spin rotation pulse with a length of 4 ps. To read if the spin was rotated from $|\uparrow\rangle$ to $|\downarrow\rangle$ state, a cw spin-pumping laser excites the system into the trion state. Following radiative recombination of a V or H-polarized photon signals the spin-rotation. The respective pulse sequence used is shown in Fig. 4b. By monitoring the emission evolution of the V-polarized $|\downarrow\uparrow\downarrow\rangle-|\uparrow\rangle$ transition we can detect the spin-rotation events as shown in the time-trace in Fig. 4c. We note here that pumping powers required for spin rotation are quite significant such that the scattered laser suppression is challenging. To take into account the non-filtered laser contribution we subtract the background by recording reference time-trace with the initial charge injection-pulse switched off. In Fig. 4d we plot the emission signal

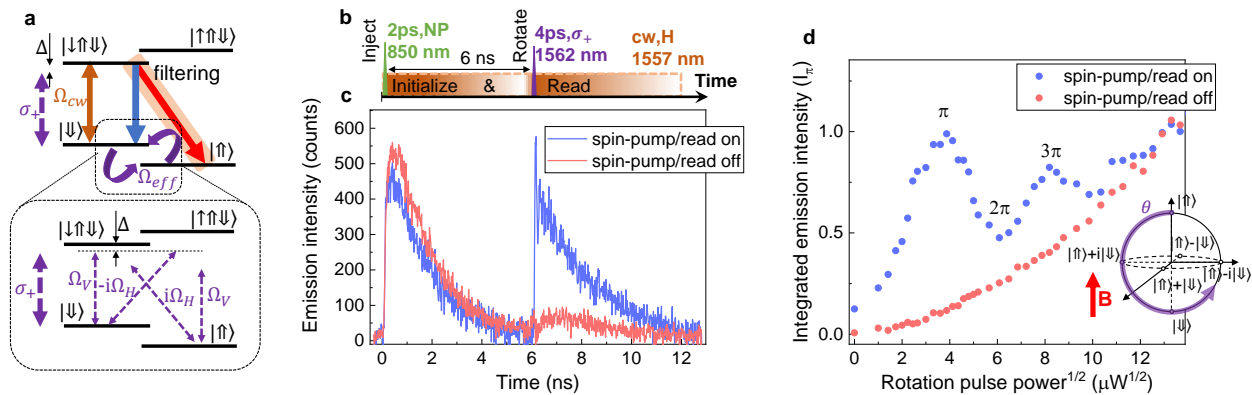


FIG. 4. **Optical coherent control of spin.** **a**, Trion level structure in Voigt magnetic field geometry with transitions relevant for the spin initialization, rotation and read-out. Inset: For the spin rotation a stimulated Raman transition using circularly polarized pulses is used which in case of small detuning can be effectively reduced to spin-rotation of a two-level system. **b**, Pulse sequence used to coherently rotate the spin. The first pulse injects the charge into the QD and a cw spin pumping laser initializes the spin into the $|\uparrow\rangle$ state. After 6 ns a circularly polarized Raman spin-rotation pulse is applied detuned by ~ 400 GHz from the trion transition. Immediately after spin-rotation into the $|\downarrow\rangle$ state, the cw laser excites the system into $|\downarrow\uparrow\downarrow\rangle$ and a photon is emitted. **c**, Emission time trace of the $|\downarrow\uparrow\downarrow\rangle$ - $|\uparrow\rangle$ transition in the presence and absence of the cw spin-pumping/read-out laser. **d**, Emission intensity after the spin-rotation pulse as a function of the square root of the rotation pulse power. Clear Rabi oscillations are visible up to 3π demonstrating coherent control. Inset: Bloch sphere representation of the hole qubit evolution with the rotation pulse power.

after the spin-rotation pulse as a function of the square root of this pulse power (blue data points). Clear oscillatory behavior can be observed, related to Rabi rotations up to 3π angle. The evolution of the Bloch vector trajectory by angle θ during this process is schematically shown in the Fig. 4d inset. To estimate the off-resonant incoherent trion excitation contribution due to the rotation pulse, we record the emission time-trace with the cw spin pumping laser switched off (red curve Fig. 4c). For the rotation powers above $100 \mu\text{W}$, the incoherent part of the emission becomes dominant over the coherent part. The oscillation amplitude damping is most likely related to the combination of a few effects, such as finite rotation pulse length in respect to Larmor period (4 vs 17.5 ps), presence of cw spin pumping/read-out laser during the spin rotation and slight tilt of the rotation vector due to the QD asymmetry and non-perfect circular polarization of the rotation pulse.

Ramsey interference and full coherent control.

To access all the qubit states on the Bloch sphere, spin rotation by a second axis is required. For that, we utilize the inherent Larmor precession of the spin state around the applied magnetic field [32]. This can be probed by the means of Ramsey interferometry. For that $|\uparrow\rangle$ population is probed after two $\pi/2$ rotation pulses separated by the variable time delay τ . The pulse sequence used and the corresponding evolution of the spin state trajectory on the Bloch sphere are shown in Fig. 5a. After a first $\pi/2$ rotation pulse, the hole spin is rotated from the north pole to the equator, where it is allowed to freely precess around the external magnetic field with a Larmor period defined by $|\downarrow\rangle$ - $|\uparrow\rangle$ splitting. By delaying a second

$\pi/2$ pulse by an amount τ , Ramsey fringes are observed. In Fig. 5b Ramsey interference for a pair $\pi/2$ pulses is shown, demonstrating integrated emission counts as a function of the time delay τ between the pulses. The data are fitted with a damped sine function exhibiting a Larmor period of 17.44 ± 0.03 ps (57.3 ± 0.2 GHz hole splitting). Additionally, in Fig. 5c the amplitude of the Ramsey fringes, as a function of the delay time between the pulses is shown. The data are fitted by an exponential decay, revealing the inhomogeneous dephasing time T_2^* of 240 ± 30 ps. While typically T_2^* on the level of nanoseconds is observed in QDs [11, 12, 33], we relate the T_2^* value recorded in our case, to the presence of the cw pumping between the rotation pulses [32], thus, T_2^* could be potentially increased by temporal modulation of the pumping laser. The fringe contrast of the first Ramsey period reaches the level of 85% (after correcting for incoherent contribution), which corresponds a $\pi/2$ rotation fidelity of 93%.

Finally, to access any arbitrary state on the Bloch sphere, we demonstrate simultaneous control of θ and ϕ rotation angles by adjusting the power of the pulses and delay time τ between them, using a pulse sequence as shown in Fig. 5d. In Fig. 5e we plot the QD integrated emission counts as a function of rotation pulse area $-\theta$ and delay time between the pulses τ . For θ increasing from 0 to $\pi/2$ the Ramsey fringe amplitude rises and achieves a maximum value at $\pi/2$. When θ is further increased from $\pi/2$ to π , the fringe amplitude decreases and a phase shift is observed. Ramsey interference fringes recorded for $\pi/2$ and π pulse areas are in clear anti-phase as shown in Fig. 5f. At $\theta = \pi$ the oscillations are sup-

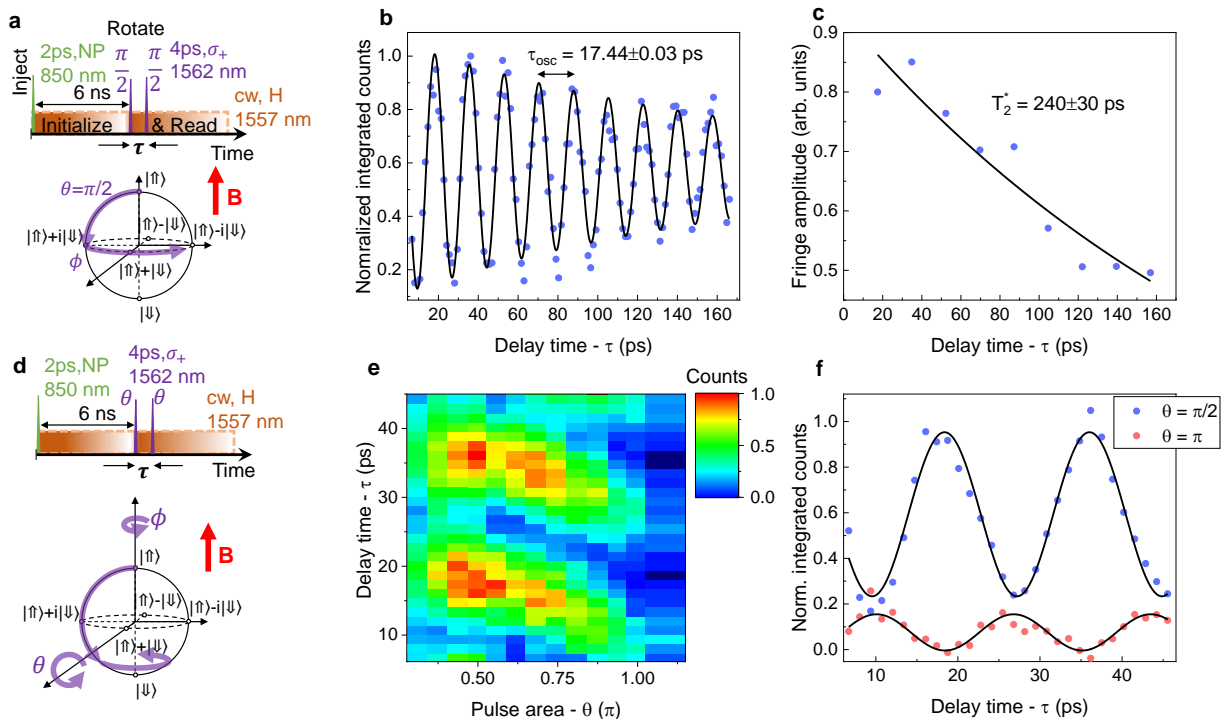


FIG. 5. Ramsey interference and full coherent control. **a**, Pulse sequence used for Ramsey interference experiment. Around 6 ns after the charge injection pulse, two Raman spin-rotation pulses with $\pi/2$ area and time delay τ are applied. The evolution of the spin-qubit state in such case is schematically represented on the Bloch sphere below. After a first $\pi/2$ rotation pulse, the hole spin is rotated from the north pole to the equator, where it is allowed to freely precess around the external magnetic field B with a Larmor period defined by the $|\downarrow\rangle$ - $|\uparrow\rangle$ splitting. By delaying a second $\pi/2$ pulse by τ , Ramsey fringes are observed. **b**, Ramsey interference for a pair of $\pi/2$ pulses, showing integrated emission counts as a function of the time delay between the pulses. The data are fitted with a damped sine function exhibiting a Larmor period of 17.44 ± 0.03 ps. **c**, The amplitude of the Ramsey fringes, as a function of the delay time between the pulses τ . Data are fitted by an exponential decay with a time constant of 240 ± 30 ps. **d**, Pulse sequence used for simultaneous control of θ and ϕ spin rotation. By changing both the delay τ and the pulse power, the entire surface of the Bloch sphere can be explored. **e**, Demonstration of full coherent control of the spin-qubit. Integrated emission counts as a function of the rotation pulse area θ and delay time between the pulses τ . **f**, Ramsey interference for a pair of $\pi/2$ and π -area pulses.

posed to vanish completely, however, some small signal is remaining. We relate this to the non-negligible spin Larmor precession with respect to the effective Rabi rotation frequency (non-zero pulse length, the QD asymmetry). Based on the recovered fringe amplitude, the extracted π rotation fidelity is 89%. Access to θ rotation in the range of 0 to π and ϕ of 0 to 2π (one Larmor period) allows to explore the entire surface of the Bloch sphere and constitutes full coherent control of the spin-qubit. Taking into account the rotation pulse length and Larmor precession period, a single gate operation within our system could be performed within a 26 ps time window.

In conclusion, we have demonstrated optical spin injection, initialization, read-out and full coherent control of a new spin-qubit system based on a hole confined in a single InAs/GaAs QD grown on a MMB layer. The measurements performed highlight this system as particularly promising for long-distance quantum network applications thanks to the possibility of interfacing spins with photons directly at C-band telecom frequencies. The QD

spin coherent control was achieved using spin rotations by two perpendicular axes using a detuned pair of picosecond pulses. Furthermore, Ramsey interferometry allowed us to probe the spin dephasing time, which in our case was limited to 240 ps due to the presence of optical pumping during the spin rotation sequence. Similar QD systems operating at shorter wavelengths and driven by modulated initialization/read-out sequences have shown the T_2^* times of over few ns [11, 12, 33]. Generating the spin-photon and spin-spin entanglement with the current device architecture should be realistically achieved in the near future. Furthermore, thanks to mature GaAs fabrication technology, our QD-spin system could be further combined with cavities and other photonic structures. This in turn might allow increasing the photon collection efficiency, speed up the spin-initialization process and achieve high optical transition cyclicality [34] for single-shot read-out. These advances combined with emission in the telecom wavelengths will be of immediate relevance for long-distance quantum networks technologies

based on optical fibres or satellites.

Methods

Sample description The QD sample used in this study was grown by metalorganic vapour phase epitaxy (MOVPE) on (100) GaAs substrate. First, the 200 nm buffer layer of GaAs was deposited, followed by 20 alternating DBR pairs of AlAs/GaAs with thickness 134.4 nm and 114.6 nm, respectively. Next, a 1080 nm thick InGaAs metamorphic buffer (MMB) layer was grown by linearly increasing the In flux over the time from 0 to 17 $\mu\text{mol}/\text{min}$. The indium concentration increase with the thickness in the MMB allows increasing the relaxation of the lattice constant. Finally, InAs material was deposited to form the QD layer, following capping with 220 nm of $\text{In}_{0.25}\text{Ga}_{0.75}\text{As}$. The bottom DBR and the top InGaAs-air interface nominally form a $3\text{-}\lambda$ cavity optimized at 1550 nm and with 100 nm stop-band width. The QD layer is placed in the cavity mode anti-node for increased photon extraction efficiency from the top. The schematic sample layer structure is shown in Fig. 1a. The QD areal density varies on the sample position and is estimated to be 10^7 cm^{-2} . More details regarding the sample fabrication process can be found in Ref. [28].

Experimental setup The sample is cooled down to a temperature of 1.6 K inside a closed-cycle liquid helium cryostat (Attodry 2100). The sample is placed in a dipstick cage-system, in which helium gas acts as an exchange gas. Superconducting magnet surrounding the sample chamber is used to apply a magnetic field up to 8 T. The optical part of the setup consists of a home-built confocal microscope mounted on top of the cryostat, and an apochromatic lens ($\text{NA} = 0.68$) inside the sample chamber. The sample is mounted on piezoelectric stages (Attocube) allowing to position the sample with respect to the lens. Non-resonant excitation of the QDs is performed using a mode-locked Ti:Sa pulsed laser (Coherent Mira) at 850 nm and 76 MHz repetition rate (2 ps pulse width). For resonant excitation, two lasers are used: (i) continuous wave tunable diode laser at 1550-1570 nm (iBlue ModBox) and (ii) tunable Optical Parametric Oscillator (Coherent OPO-X) pumped by the Ti:Sa laser at 850 nm. For the Ramsey interference experiments, a laser beam was passed through the free-space Mach-Zender interferometer where the time delay between the pulses is controlled via a retro-reflector mounted on the motorized translation stage. The fluorescence signal is collected through the same lens. A 1200 nm long-pass filter in the confocal microscope filters out the 850 nm laser excitation. Furthermore, polarization optics is set-up in cross-polarization configuration for resonant laser suppression. Additional suppression of the laser is achieved by spatial filtering using single-mode fibre. Emission is then sent to a 75 cm focal length monochromator where it could be resolved spectrally and imaged on the array detector (Princeton Instruments NIRvana) or filtered spectrally and coupled to superconducting single-photon counting

detector (Single Quantum EOS) with a time resolution better than 20 ps. The signal from the single-photon counting detectors is sent to a time-tagger module (Pico Harp 300) triggered by the laser. The total timing resolution of the setup (instrumental response function fwhm) is around 30 ps. The experimental setup scheme can be found in the Supplementary Information S1.

Data analysis The non-filtered laser contribution to the time-resolved histograms (visible under high pumping powers) is subtracted from the data by recording the reference histograms under identical conditions but with the charge injection laser (850 nm) switched off. Data shown in Fig. 5b, c, e and f are corrected for the incoherent emission contribution, decreasing the Ramsey fringes contrast from 85% to 72% under $\pi/2$ driving. The non-corrected $\pi/2$ spin rotation fidelity is 87%.

Acknowledgments We thank Yu-Ming He and Chao-Yang Lu for fruitful discussions at the beginning stages of this study. We acknowledge financial support by the German Ministry of Education and Research (BMBF) within the project "Q.Link.X" (FKZ: 16KIS0871 and 16KIS0862). We are furthermore grateful for the support by the State of Bavaria.

Author Contributions C.N., M.J., S.L.P and P.M. designed and provided the wafer. L.D. established an experimental setup, carried out the optical experiments, analyzed and interpreted the experimental data. S.H. and P.M. guided the work. L.D. wrote the manuscript with input from all authors.

Data availability The data that support the findings of this study are available from the corresponding author on reasonable request.

* lukasz@princeton.edu

- [1] H. J. Kimble, The quantum internet, *Nature* **453**, 1023 (2008).
- [2] Y.-A. Chen, Q. Zhang, T.-Y. Chen, W.-Q. Cai, S.-K. Liao, J. Zhang, K. Chen, J. Yin, J.-G. Ren, Z. Chen, S.-L. Han, Q. Yu, K. Liang, F. Zhou, X. Yuan, M.-S. Zhao, T.-Y. Wang, X. Jiang, L. Zhang, W.-Y. Liu, Y. Li, Q. Shen, Y. Cao, C.-Y. Lu, R. Shu, J.-Y. Wang, L. Li, N.-L. Liu, F. Xu, X.-B. Wang, C.-Z. Peng, and J.-W. Pan, An integrated space-to-ground quantum communication network over 4,600 kilometres, *Nature* **589**, 214 (2021).
- [3] E. Togan, Y. Chu, A. S. Trifonov, L. Jiang, J. Maze, L. Childress, M. V. G. Dutt, A. S. Sørensen, P. R. Hemmer, A. S. Zibrov, and M. D. Lukin, Quantum entanglement between an optical photon and a solid-state spin qubit, *Nature* **466**, 730 (2010).
- [4] K. De Greve, L. Yu, P. L. McMahon, J. S. Pelc, C. M. Natarajan, N. Y. Kim, E. Abe, S. Maier, C. Schneider, M. Kamp, S. Höfling, R. H. Hadfield, A. Forchel, M. M. Fejer, and Y. Yamamoto, Quantum-dot spin-photon entanglement via frequency downconversion to telecom wavelength., *Nature* **491**, 421 (2012).
- [5] W. B. Gao, P. Fallahi, E. Togan, J. Miguel-Sanchez, and

- A. Imamoglu, Observation of entanglement between a quantum dot spin and a single photon, *Nature* **491**, 426 (2012).
- [6] J. R. Schaibley, A. P. Burgers, G. A. McCracken, L. M. Duan, P. R. Berman, D. G. Steel, A. S. Bracker, D. Gammon, and L. J. Sham, Demonstration of quantum entanglement between a single electron spin confined to an InAs quantum dot and a photon, *Physical Review Letters* **110**, 1 (2013).
- [7] M. Atatüre, D. Englund, N. Vamivakas, S.-Y. Lee, and J. Wrachtrup, Material platforms for spin-based photonic quantum technologies, *Nature Reviews Materials* **3**, 38 (2018).
- [8] D. D. Awschalom, R. Hanson, J. Wrachtrup, and B. B. Zhou, Quantum technologies with optically interfaced solid-state spins, *Nature Photonics* **12**, 516 (2018).
- [9] P. Senellart, G. Solomon, and A. White, High-performance semiconductor quantum-dot single-photon sources, *Nature Nanotechnology* **12**, 1026 (2017).
- [10] P. Michler, ed., *Quantum Dots for Quantum Information Technologies*, Nano-Optics and Nanophotonics (Springer International Publishing, 2017).
- [11] A. Bechtold, D. Rauch, F. Li, T. Simmet, P.-L. Ardel, A. Regler, K. Müller, N. A. Sinitsyn, and J. J. Finley, Three-stage decoherence dynamics of an electron spin qubit in an optically active quantum dot, *Nature Physics* **11**, 1005 (2015).
- [12] R. Stockill, C. Le Gall, C. Matthiesen, L. Huthmacher, E. Clarke, M. Hugues, and M. Atatüre, Quantum dot spin coherence governed by a strained nuclear environment, *Nature Communications* **7**, 12745 (2016).
- [13] Y. He, Y.-M. He, Y.-J. Wei, X. Jiang, K. Chen, C.-Y. Lu, J.-W. Pan, C. Schneider, M. Kamp, and S. Höfling, Quantum State Transfer from a Single Photon to a Distant Quantum-Dot Electron Spin, *Physical Review Letters* **119**, 060501 (2017).
- [14] A. Delteil, Z. Sun, W.-b. Gao, E. Togan, S. Faelt, and A. Imamoglu, Generation of heralded entanglement between distant hole spins, *Nature Physics* **12**, 218 (2016).
- [15] R. Stockill, M. J. Stanley, L. Huthmacher, E. Clarke, M. Hugues, A. J. Miller, C. Matthiesen, C. Le Gall, and M. Atatüre, Phase-Tuned Entangled State Generation between Distant Spin Qubits, *Physical Review Letters* **119**, 010503 (2017).
- [16] M. H. Aboeih, J. Cramer, M. A. Bakker, N. Kalb, M. Markham, D. J. Twitchen, and T. H. Taminiau, One-second coherence for a single electron spin coupled to a multi-qubit nuclear-spin environment, *Nature Communications* **9**, 2552 (2018).
- [17] B. Hensen, H. Bernien, A. E. Dréau, A. Reiserer, N. Kalb, M. S. Blok, J. Ruitenber, R. F. L. Vermeulen, R. N. Schouten, C. Abellán, W. Amaya, V. Pruneri, M. W. Mitchell, M. Markham, D. J. Twitchen, D. Elkouss, S. Wehner, T. H. Taminiau, and R. Hanson, Loophole-free Bell inequality violation using electron spins separated by 1.3 kilometres, *Nature* **526**, 682 (2015).
- [18] W. F. Koehl, B. B. Buckley, F. J. Heremans, G. Calusine, and D. D. Awschalom, Room temperature coherent control of defect spin qubits in silicon carbide, *Nature* **479**, 84 (2011).
- [19] D. J. Christle, A. L. Falk, P. Andrich, P. V. Klimov, J. U. Hassan, N. T. Son, E. Janzén, T. Ohshima, and D. D. Awschalom, Isolated electron spins in silicon carbide with millisecond coherence times, *Nature Materials* **14**, 160 (2015).
- [20] J. M. Kindem, A. Ruskuc, J. G. Bartholomew, J. Rochman, Y. Q. Huan, and A. Faraon, Control and single-shot readout of an ion embedded in a nanophotonic cavity, *Nature* **580**, 201 (2020).
- [21] M. Raha, S. Chen, C. M. Phenicie, S. Ourari, A. M. Dibos, and J. D. Thompson, Optical quantum nondemolition measurement of a single rare earth ion qubit, *Nature Communications* **11**, 1605 (2020).
- [22] S. Chen, M. Raha, C. M. Phenicie, S. Ourari, and J. D. Thompson, Parallel single-shot measurement and coherent control of solid-state spins below the diffraction limit, *Science* **370**, 592 (2020).
- [23] M. Rančić, M. P. Hedges, R. L. Ahlefeldt, and M. J. Sellars, Coherence time of over a second in a telecom-compatible quantum memory storage material, *Nature Physics* **14**, 50 (2018).
- [24] J. F. Wang, F. F. Yan, Q. Li, Z. H. Liu, H. Liu, G. P. Guo, L. P. Guo, X. Zhou, J. M. Cui, J. Wang, Z. Q. Zhou, X. Y. Xu, J. S. Xu, C. F. Li, and G. C. Guo, Coherent Control of Nitrogen-Vacancy Center Spins in Silicon Carbide at Room Temperature, *Physical Review Letters* **124**, 223601 (2020).
- [25] L. Bergeron, C. Chartrand, A. T. K. Kurkjian, K. J. Morse, H. Riemann, N. V. Abrosimov, P. Becker, H.-J. Pohl, M. L. W. Thewalt, and S. Simmons, Silicon-Integrated Telecommunications Photon-Spin Interface, *PRX Quantum* **1**, 020301 (2020).
- [26] M. Bock, P. Eich, S. Kucera, M. Kreis, A. Lenhard, C. Becher, and J. Eschner, High-fidelity entanglement between a trapped ion and a telecom photon via quantum frequency conversion, *Nature Communications* **9**, 1998 (2018).
- [27] J. H. Weber, B. Kambs, J. Kettler, S. Kern, J. Maisch, H. Vural, M. Jetter, S. L. Portalupi, C. Becher, and P. Michler, Two-photon interference in the telecom C-band after frequency conversion of photons from remote quantum emitters, *Nature Nanotechnology* **14**, 23 (2019).
- [28] M. Paul, F. Olbrich, J. Höschele, S. Schreier, J. Kettler, S. L. Portalupi, M. Jetter, and P. Michler, Single-photon emission at 1.55 μ m from MOVPE-grown InAs quantum dots on InGaAs/GaAs metamorphic buffers, *Applied Physics Letters* **111**, 033102 (2017).
- [29] C. Carmesin, F. Olbrich, T. Mehrtens, M. Florian, S. Michael, S. Schreier, C. Nawrath, M. Paul, J. Höschele, B. Gerken, J. Kettler, S. L. Portalupi, M. Jetter, P. Michler, A. Rosenauer, and F. Jahnke, Structural and optical properties of InAs/(In)GaAs/GaAs quantum dots with single-photon emission in the telecom C-band up to 77 K, *Physical Review B* **98**, 125407 (2018).
- [30] M. Atatüre, J. Dreiser, A. Badolato, A. Högele, K. Karrai, and A. Imamoglu, Quantum-dot spin-state preparation with near-unity fidelity, *Science* **312**, 551 (2006).
- [31] B. D. Gerardot, D. Brunner, P. A. Dalgarno, P. Öhberg, S. Seidl, M. Kroner, K. Karrai, N. G. Stoltz, P. M. Petroff, and R. J. Warburton, Optical pumping of a single hole spin in a quantum dot, *Nature* **451**, 441 (2008).
- [32] D. Press, T. D. Ladd, B. Zhang, and Y. Yamamoto, Complete quantum control of a single quantum dot spin using ultrafast optical pulses, *Nature* **456**, 218 (2008).
- [33] K. De Greve, P. L. McMahon, D. Press, T. D. Ladd, D. Bisping, C. Schneider, M. Kamp, L. Worschech, S. Höfling, A. Forchel, and Y. Yamamoto, Ultrafast co-

- herent control and suppressed nuclear feedback of a single quantum dot hole qubit, [Nature Physics](#) **7**, 872 (2011).
- [34] M. H. Appel, A. Tiranov, A. Javadi, M. C. Löbl, Y. Wang, S. Scholz, A. D. Wieck, A. Ludwig, R. J. Warburton, and P. Lodahl, Coherent Spin-Photon Interface with Waveguide Induced Cycling Transitions, [Physical Review Letters](#) **126**, 013602 (2021).

Supplementary Information: Optical Charge Injection and Full Coherent Control of Spin-Qubit in the Telecom C-band Emitting Quantum Dot

Lukasz Dusanowski,^{1,2,*} Cornelius Nawrath,³ Simone L. Portalupi,³ Michael Jetter,³ Tobias Huber,¹ Sebastian Klemmt,¹ Peter Michler,³ and Sven Höfling^{1,4}

¹*Technische Physik and Würzburg-Dresden Cluster of Excellence ct.qmat,
University of Würzburg, Physikalisches Institut and Wilhelm-Conrad-Röntgen-Research
Center for Complex Material Systems, Am Hubland, D-97074 Würzburg, Germany*

²*currently at: Department of Electrical Engineering,
Princeton University, Princeton, NJ 08544, USA*

³*Institut für Halbleiteroptik und Funktionelle Grenzflächen (IHFG),
Center for Integrated Quantum Science and Technology (IQST) and SCoPE,
University of Stuttgart, D-70569 Stuttgart, Germany*

⁴*SUPA, School of Physics and Astronomy, University of St Andrews, KY16 9SS St Andrews, UK*

Keywords: spin control, hole qubit, quantum dot, telecom C-band

CONTENT DESCRIPTION

In this supplementary information document, we provide further details on the experimental setup scheme (S1), non-resonant photoluminescence at $B = 0$ (S2), magneto-photoluminescence (S3), and the rate-equation model (S4).

S1: EXPERIMENTAL SETUP

For all experiments, the sample is kept in a low-vibration closed-cycle magneto-cryostat (attoDRY2100) at a temperature of ~ 1.6 K. A superconducting magnet surrounding the sample chamber is used to apply a magnetic field up to 8 T. The optical part of the setup consists of a home-built confocal microscope mounted on top of the cryostat, and an apochromatic lens with a numerical aperture NA of 0.68. The sample is mounted on piezoelectric stages (Attocube) for control of its position with respect to the lens. Non-resonant excitation of QDs is performed using a pulsed mode-locked Ti:Sa laser (Coherent Mira) at 850 nm and 76 MHz repetition rate (2 ps pulse width). For resonant excitation, two lasers are used: (i) a continuous wave tunable diode laser at 1550-1570 nm (iBlue ModBox) and (ii) a tunable Optical Parametric Oscillator (Coherent OPO-X) pumped by the Ti:Sa laser at 850 nm. The OPO generated optical pulses are shaped spectrally using a fiber-based tunable grating band-pass filter with adjustable bandwidth (EXFO XTM-50). For the Ramsey interference experiments, a laser beam is passed through the free-space Mach-Zender interferometer where the time delay between the pulses is controlled via a retro-reflector mounted on the motorized translation stage. The fluorescence signal is collected through the same lens. A 1200 nm long-pass filter in the confocal microscope filters out the 850 nm laser excitation. Furthermore, polarization optics is set-up in cross-polarization configuration for resonant laser suppression. Additional suppression of the laser is achieved by spatial filtering using single-mode fiber. Emission is then sent to a 75 cm focal length monochromator where it could be resolved spectrally and imaged on the array detector (Princeton Instruments NIRvana) or filtered spectrally and coupled into a superconducting single-photon counting detector (SSPCD, Single Quantum EOS). The SSPCD time resolution is better than 20 ps, the quantum efficiency is over 70%, and the dark count rate is around 100-200 cps. The signal from the single-photon counting detectors is sent to a time-to-digital converter module (Pico Harp 300) triggered by the laser. The total timing resolution of the setup (instrumental response function fwhm) is around 30 ps. The spectroscopic configuration used is shown schematically in Fig. S1.

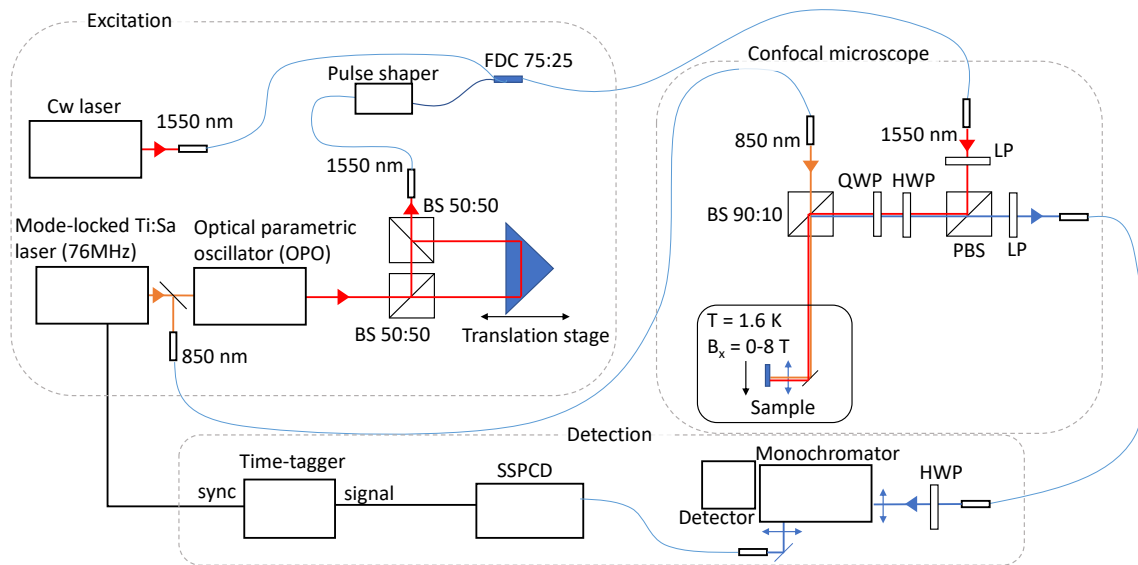


FIG. S1. **Experimental setup scheme.** The sample is kept in a low-vibration closed-cycle magneto-cryostat at a temperature of ~ 1.6 K. For optical excitation and PL signal collection, we use an apochromatic lens mounted on a periscope inside the sample chamber. Non-resonant excitation is performed using a pulsed mode-locked Ti:Sa laser at 850 nm and 76 MHz repetition rate (2 ps pulse width). For resonant excitation a continuous-wave tunable diode laser at 1550-1570 nm and a tunable Optical Parametric Oscillator (OPO) pumped by the Ti:Sa laser is used. For the Ramsey interference experiments, a laser beam is passed through a free-space Mach-Zender interferometer, where the time delay is controlled via a retro-reflector mounted on the motorized translation stage. For polarization control, a half-wave plate (HWP) and a quarter-wave plate (QWP) combined with a linear polarizer (LP) are used, set-up in cross-polarization configuration for resonant laser suppression. Emission collected into the single-mode fiber is sent to a 75 cm focal length monochromator where it is resolved spectrally and imaged on the array detector. Alternatively, a signal is filtered spectrally and coupled into a superconducting single-photon counting detector (SSPCD). The electronic signal from the SSPCD is sent to the time-tagger module synchronized with the laser.

S2: NON-RESONANT PHOTOLUMINESCENCE AT $B = 0$

In Fig. S2 a polarization-resolved zero-field PL spectrum of the investigated quantum dot is shown under non-resonant, pulsed excitation at 850 nm. For that, a half-wave-plate is rotated placed before a fixed linear polarizer located in front of the signal detection fiber (see Fig. S1). The investigated line does not show any polarization splitting within setup resolution and exhibits slight linear polarization with a degree of 11%, which we attribute to the light-hole-heavy-hole bands mixing. More detailed experimental and theoretical studies of excitonic transitions in investigated InAs MMB QDs are summarized in Ref. [?] and indicate a dominant contribution of positively charged complexes in the emission spectra. Following on the above observations and earlier studies we attribute the investigated emission line to a positively charged exciton.

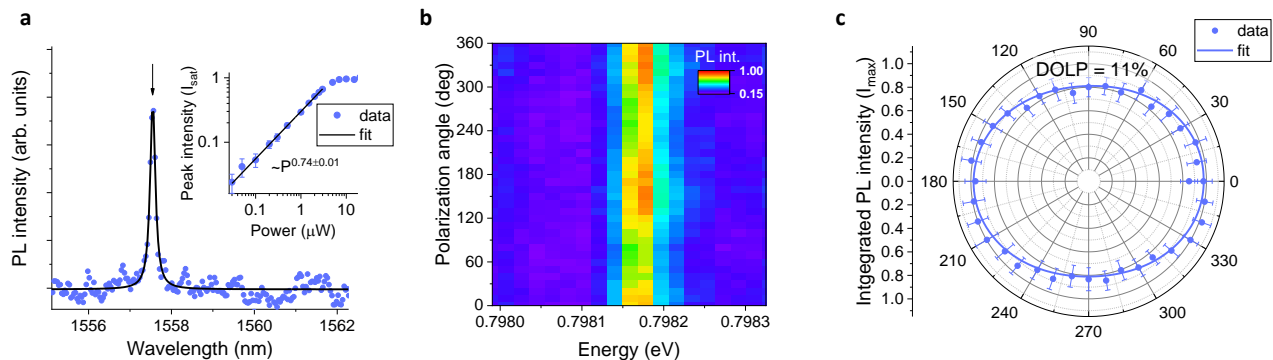


FIG. S2. **Non-resonant photoluminescence.** (a) Low temperature (1.6 K) photoluminescence spectrum of the investigated QD under pulsed 850 nm excitation. The emission line identified as a positive trion is marked with an arrow and fit using Lorentzian function. Inset: PL intensity vs laser pumping power dependence. (b) Color coded PL emission spectra versus detection linear polarization angle. Polarization splitting is not observed for the investigated line within the setup resolution. (c) Polar plot of investigated line emission intensity versus detection linear polarization angle. Line exhibits slight linear polarization with a degree of 11% (most likely due to the light-hole-heavy-hole bands mixing).

S3: MAGNETO-PHOTOLUMINESCENCE

In Fig. S3a photoluminescence spectra of the investigated QD are shown in function of the applied magnetic field. Data is recorded for H and V polarizations under magnetic field up to 7 T in Voigt configuration. Clear four-fold line splitting can be observed, which is characteristic for the trion and following selection rules shown in Fig. 1b in the main text. Particular transition peaks are fit using Lorentzian function and derived energy shifts in respect to zero magnetic field plotted in Fig. S3b. By calculating the energy splitting between H and V polarized peaks, we recover the Zeeman splitting as shown in Fig. S3c. By performing a linear fit to the data, we recover the g-factors g_V and g_H of 2.54 and 2.86, respectively. This in turn allows us to estimate the ground-state spin g-factor to be 2.7, and the excited-state-spin g-factor to be 0.16. In Fig. S3d, we plot the diamagnetic shift vs applied magnetic field, calculated as mean energy of the split lines averaged over V and H polarization. Data are fit using quadratic function and allowed to extract a diamagnetic shift coefficient of $8.2 \mu\text{eV}/\text{T}^2$.

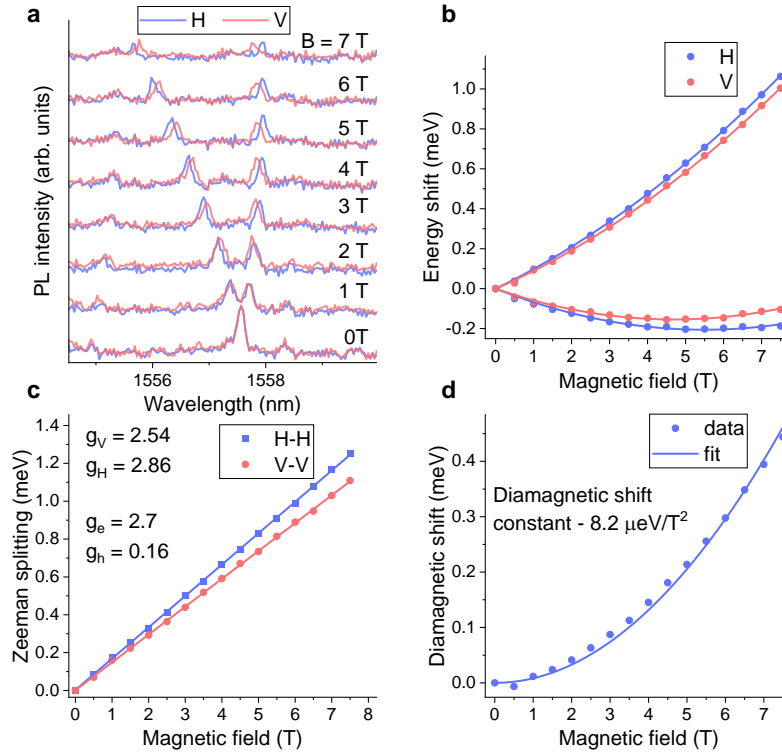


FIG. S3. **Voigt configuration magneto-photoluminescence.** (a) Photoluminescence spectra at various magnetic fields up to 7 T recorded under horizontal (H) and vertical (V) linear polarization. (b) Energy shift of the optical transitions versus applied magnetic field. A magnetic field is applied in the Voigt configuration. (c) Zeeman splitting between V and H-polarized transitions vs applied magnetic field revealing excited and ground-state spin g-factors of 0.16 and 2.7, respectively. (d) Diamagnetic shift vs applied magnetic field. By performing quadratic function fit, a diamagnetic shift constant of $8.2 \mu\text{eV}/\text{T}^2$ was designated.

S4: RATE-EQUATION MODEL

To fit the data in Fig. 3e in the main text we theoretically model the dynamics of the spin-initialization process in our system using a rate-equation model. For that, we consider four levels: two trion states $|\uparrow\uparrow\downarrow\rangle$, $|\downarrow\uparrow\downarrow\rangle$, and two ground spin states $|\uparrow\rangle$ and $|\downarrow\rangle$. We describe the time evolution of particular states populations $n_{|\uparrow\uparrow\downarrow\rangle}(t)$, $n_{|\downarrow\uparrow\downarrow\rangle}(t)$, $n_{|\uparrow\rangle}(t)$ and $n_{|\downarrow\rangle}(t)$ using following rate-equations:

$$\frac{d}{dt}n_{|\uparrow\uparrow\downarrow\rangle}(t) = -2n_{|\uparrow\uparrow\downarrow\rangle}(t)\Gamma + n_{|\uparrow\rangle}(t)R_p + n_{|\downarrow\uparrow\downarrow\rangle}(t)\gamma_e - n_{|\uparrow\uparrow\downarrow\rangle}(t)\gamma_e, \quad (1)$$

$$\frac{d}{dt}n_{|\downarrow\uparrow\downarrow\rangle}(t) = -2n_{|\downarrow\uparrow\downarrow\rangle}(t)\Gamma + n_{|\uparrow\uparrow\downarrow\rangle}(t)\gamma_e - n_{|\downarrow\uparrow\downarrow\rangle}(t)\gamma_e, \quad (2)$$

$$\frac{d}{dt}n_{|\uparrow\rangle}(t) = n_{|\uparrow\uparrow\downarrow\rangle}(t)\Gamma + n_{|\downarrow\uparrow\downarrow\rangle}(t)\Gamma - n_{|\uparrow\rangle}(t)R_p + n_{|\downarrow\rangle}(t)\gamma_h - n_{|\uparrow\rangle}(t)\gamma_h, \quad (3)$$

$$\frac{d}{dt}n_{|\downarrow\rangle}(t) = n_{|\uparrow\uparrow\downarrow\rangle}(t)\Gamma + n_{|\downarrow\uparrow\downarrow\rangle}(t)\Gamma + n_{|\uparrow\rangle}(t)\gamma_h - n_{|\downarrow\rangle}(t)\gamma_h, \quad (4)$$

where Γ is trion spontaneous recombination rate, R_p is spin pumping rate proportional to the pumping power, γ_e is trion electron spin-flip rate and γ_h is hole spin-flip rate (lifetime of the ground spin state). We solve the equations numerically assuming that after the charge injection pulse, the system is prepared in the random trion state, such that initial populations are $n_{|\uparrow\uparrow\downarrow\rangle}(0) = 0.5$, $n_{|\downarrow\uparrow\downarrow\rangle}(0) = 0.5$, $n_{|\uparrow\rangle}(0) = 0$ and $n_{|\downarrow\rangle}(0) = 0$. To fit the data in the Fig. 3e in the main text, we calculate the $|\uparrow\rangle$ and $|\downarrow\rangle$ states populations $n_{|\uparrow\rangle}(t)$ and $n_{|\downarrow\rangle}(t)$ at the time t equal to 4.5 ns, and plot them in function of the spin-pumping-rate for various values of spin-flip rates and fixed to $1/1.4 \text{ ns}^{-1}$ spontaneous emission rate (taken from a time-resolved experiments). We found that good fit to the experimental data is achieved for $1/\gamma_h$ values above 400 ns, which sets the lower limit of the hole spin lifetime in our QDs, and is also similar to previously reported values of 100 ns to 10 ms [? ? ?] in 800-1000 nm emitting InAs/GaAs self-assembled QDs. We also found that the trion spin-flip rate γ_e does not influence the $n_{|\uparrow\rangle}(t)$ evolution so that we fix it to 1 ns^{-1} . In Fig. S4a we show simulated initialization fidelity after 4.5 ns spin-pumping time and in Fig. S4b time evolution of spin $|\uparrow\rangle$ population during the optical pumping process. From graph b we can extract the theoretical spin-initialization fidelity of 96% and 99% after 4.5 ns and 6 ns optical spin-pumping time, respectively.

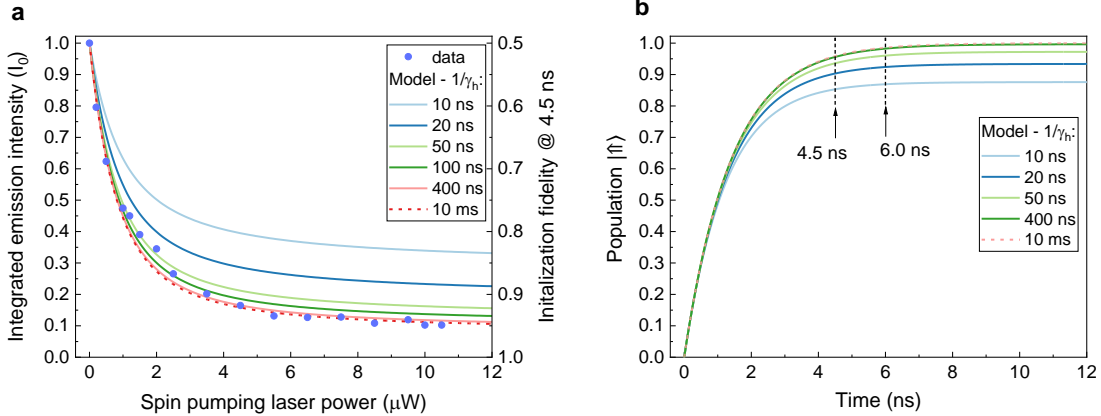


FIG. S4. **Spin initialization fidelity and dynamics.** (a) Spin initialization fidelity vs spin-pumping laser power calculated for various spin-flip rates. Simulations are performed for 4.5 ns optical pumping time. Equally good fit is obtained for $1/\gamma_h$ in the range of 400 ps to 10 ms. (b) Time evolution of spin $|\uparrow\rangle$ population during the optical pumping process for various hole spin-flip rates γ_h . Simulations are performed for optical spin-pumping rate well above the saturation value ($1/R_p = 100 \text{ ns}^{-1}$).